Monthly Notices of the ROYAL ASTRONOMICAL SOCIETY

MNRAS **519,** 5149–5160 (2023) https://doi.org/10.1093/mnras/stac3664
Advance Access publication 2022 December 15

The X-ray view of optically selected dual AGN

Alessandra De Rosa [1]★ Cristian Vignali [2,3]★ Paola Severgnini [4]★ Stefano Bianchi [5] Tamara Bogdanović,[6] Maria Charisi,[7] Matteo Guainazzi,[8] Zoltan Haiman,[9] S. Komossa,[10] Zsolt Paragi [11,12] Miguel Perez-Torres,[13] Enrico Piconcelli,[14] Lorenzo Ducci,[15] Manali Parvatikar[15] and Roberto Serafinelli[1]

[1]*INAF – Istituto di Astrofisica e Planetologia Spaziali (IAPS), via Fosso del Cavaliere, Roma I-133, Italy*
[2]*Dipartimento di Fisica e Astronomia 'Augusto Righi', Università degli Studi di Bologna, Via Gobetti 93/2, 40129 Bologna, Italy*
[3]*INAF – Osservatorio di Astrofisica e Scienza dello Spazio di Bologna, Via Gobetti 93/3, 40129 Bologna, Italy*
[4]*INAF – Osservatorio Astronomico di Brera, via Brera 28, I-20121, Milano, Italy*
[5]*Dipartimento di Matematica e Fisica, Università degli Studi Roma Tre, via della Vasca Navale 84, 00146 Roma, Italy*
[6]*School of Physics and Center for Relativistic Astrophysics, Georgia Institute of Technology, Atlanta, GA 30332, USA*
[7]*Department of Physics and Astronomy, Vanderbilt University, 2301 Vanderbilt Place, Nashville, TN 37235, USA*
[8]*ESA – European Space Research and Technology Centre (ESTEC), Keplerlaan 1, 2201AZ Noordwijk, The Netherlands*
[9]*Department of Astronomy, Columbia University, New York, NY 10027, USA*
[10]*Max-Planck-Institut für Radioastronomie, Auf dem Hügel 69, 53121 Bonn, Germany*
[11]*Department of Experimental Physics, University of Szeged, Dóm tér 9, H-6720 Szeged, Hungary*
[12]*Joint Institute for VLBI ERIC, Postbus 2, NL-7900 AA Dwingeloo, The Netherlands*
[13]*Centro de Estudios de la Física del Cosmos de Aragón (CEFCA), 44001 Teruel, Spain*
[14]*INAF − Osservatorio Astronomico di Roma, via Frascati 33, 00040 Monte Porzio Catone (Roma), Italy*
[15]*Institut für Astronomie und Astrophysik, Kepler Center for Astro and Particle Physics, Universität Tübingen, Sand 1, 72076 Tübingen, Germany*

Accepted 2022 December 6. Received 2022 November 14; in original form 2022 October 10

ABSTRACT

We present a study of optically selected dual Active Galactic Nuclei (AGN) with projected separations of 3–97 kpc. Using multiwavelength (MWL) information (optical, X-ray, mid-IR), we characterized the intrinsic nuclear properties of this sample and compared them with those of isolated systems. Among the 124 X-ray-detected AGN candidates, 52 appear in pairs and 72 as single X-ray sources. Through MWL analysis, we confirmed the presence of the AGN in >80 per cent of the detected targets in pairs (42 out of 52). X-ray spectral analysis confirms the trend of increasing AGN luminosity with decreasing separation, suggesting that mergers may have contributed to triggering more luminous AGN. Through X-ray/mid-IR ratio versus X-ray colours, we estimated a fraction of Compton-thin AGN (with 10^{22} cm^{-2} < $N_{\rm H}$ < 10^{24} cm^{-2}) of about 80 per cent, while about 16 per cent are Compton-thick sources (with $N_{\rm H} > 10^{24}$ cm^{-2}). These fractions of obscured sources are larger than those found in samples of isolated AGN, confirming that pairs of AGN show higher obscuration. This trend is further confirmed by comparing the de-reddened [O III] emission with the observed X-ray luminosity. However, the derived fraction of Compton-thick sources in this sample at the early stages of merging is lower than that reported for late-merging dual-AGN samples. Comparing $N_{\rm H}$ from X-rays with that derived from $E(B-V)$ from narrow-line regions, we found that the absorbing material is likely to be associated with the torus or broad-line regions. We also explored the X-ray detection efficiency of dual-AGN candidates, finding that, when observed properly (at on-axis positions and with long exposures), X-ray data represent a powerful way to confirm and investigate dual-AGN systems.

Key words: galaxies: active – galaxies: Seyfert – galaxies: interactions – X-rays: general – infrared: galaxies.

1 INTRODUCTION

Dual Active Galactic Nuclei (AGN), with separations of 100 pc–100 kpc, have been subject of interest owing to their connection with Massive Black Holes (MBHs) triggering through mergers (Di Matteo, Springel & Hernquist 2005; Treister et al. 2012) and as a precursor of MBHs coalescence (Amaro-Seoane et al. 2022 and references therein). Dual AGN are hard to detect (see De Rosa et al. 2019 for a review on observational and theoretical issues). Different techniques are used to select AGN pair candidates in different wavebands (Burke-Spolaor 2011; Comerford et al. 2012; Fu et al. 2015; Foord et al. 2020; Mannucci et al. 2022). Most published samples are sparse and not homogeneous and need to be confirmed through further multiwavelength (MWL) observational programs. Dual AGN at the early stage of galaxy mergers (1–10 kpc scale) have been identified mostly serendipitously (Komossa

★ E-mail: alessandra.derosa@inaf.it (ADR); cristian.vignali@unibo.it (CV); paola.severgnini@inaf.it (PS)

et al. 2003; Ballo et al. 2004; Bianchi et al. 2008; Guainazzi et al. 2005; Piconcelli et al. 2010). Several studies have been performed at low redshift, mainly through large surveys in the optical, X-ray, and IR (Koss et al. 2010; Comerford et al. 2012; Liu et al. 2011; Ricci et al. 2017). It has also been shown that higher-luminosity AGN are found in interacting systems and that average luminosity increases with decreasing separation (Hou, Li & Liu 2020; Satyapal et al. 2014; Koss et al. 2012; Kocevski et al. 2012; Silverman et al. 2011), suggesting that mergers may trigger MBH activity (Di Matteo et al. 2005; Treister et al. 2012). In this scenario of merger-triggered accretion, it is expected that MBHs are completely obscured by gas and dust during the final stage of merging (Hopkins et al. 2006).

Both cosmological and numerical simulations have investigated the dynamics and physics of merging MBHs, identifying several parameters that contribute in the activation of both MBHs at the same time (galaxy mass ratio, MBH orbital parameters) and the properties of the environment during the merger (Volonteri et al. 2022; Blecha et al. 2018; Capelo et al. 2017). Although observations have shown that AGN in mergers are characterized by higher obscuration compared with isolated AGN (Ricci et al. 2021; Guainazzi et al. 2021; Pfeifle et al. 2019; De Rosa et al. 2018; Satyapal et al. 2017; Ricci et al. 2017; De Rosa et al. 2015; Kocevski et al. 2015), as expected from simulations, it still remains unclear how this obscuration evolves along the merger phase.

It is therefore essential to identify from theory and simulations the observational signatures to be compared with real observations and to track the evolution of MBH along the different coalescence phases. To take a step forward with this research, we need a statistically significant sample of dual AGN covering a wide dynamical range in spatial separations (1–100 kpc scale). Sloan Digital Sky Survey (SDSS) offers a huge pool of optical data to extract good dual-AGN candidates through imaging (for spatially resolved systems) and spectroscopy (for spatially unresolved systems), the so-called double-peaked AGN (Wang et al. 2009; Ge et al. 2012; Smith et al. 2010; Kim et al. 2020). The double-peaked technique assumes that each AGN in the system carries its own narrow-line region (NLR) tracing the systemic velocity of the AGN as they move in their common gravitational potential. However, when the nature of the candidates are verified through MWL observations, only a tiny fraction, about 2 per cent, can be confirmed as dual AGN. This is due to the fact that the signature (i.e. the presence of a doubled-peaked profile) is not unique, indicating other possible effects originating near a single AGN (e.g. matter outflows); furthermore, the classification of a galaxy as an AGN is not easy owing to extinction (Severgnini, Caccianiga & Della Ceca 2012) and/or the presence of emission from star-forming (SF) regions.

X-rays represent an efficient technique to detect and confirm accretion-dominated sources such as AGN, even in the case of moderate absorption (i.e. Compton-thin; column density $N_H \leq 10^{24}$ cm^{-2}). When used together with other diagnostics, for example mid-IR emission, even heavily obscured systems can be detected through their X-ray luminosity.

With the main objective of characterizing a homogeneous sample of dual AGN at kiloparsec separation, and of comparing their properties with isolated AGN, in this paper we present an X-ray study of a sample of optically selected dual AGN with separations in the range 3–97 kpc. We analysed the X-ray archival data from *XMM–Newton* and *Chandra*, making use of target selection in 4XMM (the XMM-Newton serendipitous source catalogue, Webb et al. 2020) and CSC2 (The Chandra Source Catalog, Evans et al. 2020, 2010). The paper is structured as follows. In Section 2 we present the sample and its selection, while the MWL data analysis is presented in Section 3. The diagnostic tools used to identify AGN are described in Section 4. We discuss our main results in Section 5 and provide a summary in Section 6. Throughout the paper we adopt a concordance cosmology with $H_0 = 70$ km s^{-1} Mpc^{-1}, $\Omega_\Lambda = 0.7$, $\Omega_M = 0.3$. Errors and upper limits quoted in the paper correspond to the 90 per cent confidence level, unless noted otherwise.

2 SAMPLE SELECTION

We considered the optically selected (SDSS) dual AGN from Liu et al. (2011), containing 2488 AGN in pairs (1244 systems at $\bar{z} \sim 0.1$ with line-of-sight velocity offsets $\Delta v < 600$ km s^{-1} and projected separations < 100 h$_{70}^{-1}$ kpc). Among these targets, 302 fall in the sky regions covered by *Chandra* and/or *XMM–Newton* (considering off-axis positions lower than 10 and 15 arcmin for *Chandra* and *XMM–Newton*, respectively, and exposure longer than 10 ks); the X-ray detection efficiency will be thoroughly investigated in Section 5.2. The optical catalogue was cross-correlated with 4XMM-DR10 (Webb et al. 2020), considering a match position in a circle with a 5-arcsec radius (which considers the *XMM–Newton* telescope position accuracy), resulting in 73 sources. Among these 73 sources, 37 appear as single AGN (7 from 37 with angular separation below 15 arcsec) and 36 appear in pairs (hence, 18 dual-AGN systems). The main properties of the 18 AGN pairs are reported in the first block of Table 1. Owing to the *XMM–Newton* spatial resolution and the redshift of the optical sample, the minimum projected separation we are able to explore is 7 kpc. In order to populate the sample with systems at closer separations, we performed the same selection using *Chandra* observations. We used the CSC2 catalogue (Evans et al. 2020, 2010), obtaining 51 additional targets with projected separation in the range 3–71 kpc. A total of 16 CSC2 targets are in eight pairs (see the second block of Table 1), while 35 sources appear as single AGN. The spectral analysis of CSC2 targets has been reported in the literature only for a few sources. However, for the sake of uniformity in the analysis, we re-analysed all of the sources.

The final cross-match between optical and X-ray catalogues returns 124 targets (73 in 4XMM and 51 in CSC2): 52 of them appear in 26 dual systems with separations of 3.4–97.2 kpc (see Table 1). We note that the mean value and distribution of projected separations between the X-ray-detected targets and the parent population from Liu et al. (2011) are in a good agreement (51 versus 58 kpc), although with a large dispersion (standard deviation of 30 versus 29 kpc).

For all detected targets, we also searched for mid-IR information. In this regard, the Wide-field Infrared Survey Explorer catalogue (AllWISE, Wright et al. 2010) provides the magnitudes in the Vega photometric system acquired in the four observational bands of WISE (W1 = 3.4 μm, W2 = 4.6 μm, W3 = 12 μm, W4 = 22 μm). To obtain flux densities, we used the conversion as in Jarrett et al. (2011), namely $F_\nu[Jy] = F_{\nu_O} \times 10^{-(m_{\rm Vega}/2.5)}$, where F_{ν_O} is the zero-magnitude flux density corresponding to the constant that gives the same response as that of Vega.

For 32 targets (4XMM: 17, CSC2: 15), we reached a sufficient signal-to-noise (S/N) ratio to enable X-ray spectral analysis. This threshold was chosen as ~ 100 cts for 4XMM-EP8 in the band (0.2–12 keV), while in the case of *Chandra* we used the spectra released in CSC2 (see details in Evans et al. 2020). In the following section, we explore different diagnostics using a MWL approach in order to confirm the AGN nature for the 26 dual-AGN systems selected optically. The properties of the optically dual AGN detected as single

Table 1. Dual-AGN candidates detected in 4XMM and CSC2. Numbering in the first column refers to the sources shown in Fig. 1.

	Obs. ID	Simbad name (SDSS)	RA (°)	Dec. (°)	z	[(1)]Sep. (arcsec)	[(2)]rp (kpc)	IAU name (4XMM/2CXO)	[(3)]Net counts (counts)	Ref.
					XMM–Newton					
1	0761730401	J015235.35–083236.6	28.14729	− 8.5435	0.0517	58.5	58.9	J015235.2-083233	73 ± 13	
2	0761730401	J015235.99–083138.9	28.14996	− 8.52747	0.0511	58.5	58.9	J015235.9-083139	69 ± 12	
3	0741580501	J082321.66+042220.9	125.84029	4.37247	0.0311	142.8	88.7	J082321.6+042221	8871 ± 125	H20
4	0741580501	J082329.87+042332.9	125.8745	4.3925	0.0308	142.8	88.7	J082329.9+042332	39 ± 10	H20
5	0740620201	J083157.64+191241.4	127.99021	19.21153	0.0372	55.8	41.2	J083157.6+191241	149 ± 21	
6	0740620201	J083200.51+191205.8	128.00212	19.20164	0.0375	55.8	41.2	J083200.6+191206	86 ± 13	
7	0743110701	J100133.68+033731.1	150.39033	3.62533	0.0437	53.8	45.3	J100133.4+033731	314 ± 48	
8	0743110701	J100135.80+033647.8	150.39921	3.61328	0.0427	53.8	45.3	J100135.8+033648	260 ± 29	
9	0503600301	J100230.89+324252.3	150.62871	32.71456	0.049	89.3	88.1	J100230.8+324248	71 ± 15	
10	0503600301	J100236.54+324224.2	150.65225	32.70675	0.0505	89.3	88.1	J100236.6+324224	2359 ± 93	
11	0146990101	J102141.89+130550.3	155.42454	13.09733	0.0765	67.1	97.2	J102141.8+130551	45 ± 11	H20
12	0146990101	‡*J102142.78+130656.1*	155.42829	13.11558	0.0763	67.1	97.2	J102142.6+130654	179 ± 17	H20
13	0692330501	‡*J112545.04+144035.6*	171.43771	14.67658	0.034	73.6	49.7	J112545.1+144035	622 ± 30	H20, TA18
14	0692330501	J112549.54+144006.5	171.45646	14.6685	0.0339	73.6	49.7	J112549.5+144006	249 ± 21	H20, TA18
15	0555060501	J120157.72+295926.6	180.4905	29.99075	0.072	19.1	25.9	J120157.8+295927	62 ± 11	
16	0555060501	J120157.88+295945.5	180.49117	29.996	0.0713	19.1	25.9	J120157.8+295945	40 ± 10	
17	0601780601	J120443.31+311038.2	181.1805	31.17728	0.025	61.5	31.0	J120443.3+311037	16517 ± 137	K10
18	0601780601	J120445.19+311132.9	181.18833	31.19247	0.025	61.5	31.0	J120445.3+311130	154 ± 20	K10
19	0111281601	J134130.40–002514.3	205.37671	− 0.42072	0.0713	61.5	83.6	J134130.5-002512	30 ± 9	
20	0111281601	J134133.37-002432.0	205.38904	− 0.40892	0.0719	61.5	83.6	J134133.4-002431	42 ± 9	
21	0783520501	J145627.39+211955.9	224.11417	21.33222	0.0443	68.4	59.2	J145627.4+211956	†602 ± 25	ADR18
22	0783520501	J145631.35+212030.0	224.13067	21.34169	0.044	68.4	59.2	J145631.3+212030	†459 ± 32	ADR18
23	0721820201	J145838.58+382727.9	224.66075	38.45775	0.1358	32.6	78.8	J145838.5+382727	124 ± 16	
24	0721820201	J145840.73+382732.7	224.66971	38.45908	0.1367	32.6	78.8	J145840.6+382730	73 ± 16	
25	0147210301	J160501.37+174632.4	241.25571	17.77569	0.033	117.3	78.1	J160501.3+174632	77 ± 14	H20,
26	0147210301	J160507.88+174527.6	241.28287	17.75767	0.0334	117.3	78.1	J160508.1+174528	109 ± 27	H20,
27	0783520301	J162640.93+142243.6	246.67054	14.37878	0.0479	54.1	51.3	J162640.9+142243	†364 ± 20	ADR18
28	0783520301	J162644.50+142250.6	246.68546	14.38075	0.0484	54.1	51.3	J162644.4+142253	†162 ± 15	ADR18
29	0784521201	J163102.72+394733.0	247.76133	39.7925	0.0289	165.8	96.0	J163102.7+394733	345 ± 28	
30	0784521201	J163103.40+395018.5	247.76421	39.83847	0.0305	165.8	96.0	J163103.4+395015	85 ± 17	
31	0673000147	J221839.91–002402.0	334.66633	− 0.40053	0.0948	30.7	54.2	J221839.8-002400	38 ± 10	
32	0673000147	‡*J221840.97–002335.5*	334.67071	− 0.39319	0.095	30.7	54.2	J221840.9-002333	20 ± 8	
33	0783520101	J094554.40+423839.9	146.47671	42.6444	0.0745	21.3	30.3	J094554.4+423839	†21450 ± 150	ADR18
34	0783520101	J094554.49+423818.7	146.47701	42.6385	0.0745	21.3	30.3	J094554.4+423839	†1275 ± 37	ADR18
35	0783520201	J103853.29+392151.1	159.72204	39.36422	0.0548	40.4	42.9	J103853.3+392151	†6534 ± 80	ADR18
36	0783520201	J103855.94+392157.5	159.73312	39.36660	0.0548	40.4	42.9	J103855.9+392157	†182 ± 14	ADR18
					Chandra					
1	14965	J090714.44+520343.4	136.81021	52.06206	0.0596	7.6	8.9	J090714.4+520343	$41.9^{+7.2}_{-6.5}$	H19,H20
2	14965	J090714.61+520350.6	136.81087	52.06408	0.0602	7.6	8.9	J090714.6+520350	$120.9^{+11.6}_{-11.5}$	H19,H20
3	4110, 4934	J121345.92+024838.9	183.44146	2.81083	0.073	3.4	4.8	J121345.9+024838	$11.3^{+4.}_{-3.4}$	H20,I11,R21
4	4110, 4934	J121346.07+024841.4	183.44212	2.8115	0.0731	3.4	4.8	J121346.0+024841	$14.9^{+4.5}_{-3.9}$	H20,I11,R21
5	2043	‡*J124610.10+304354.9*	191.54212	30.73192	0.0219	37.2	16.4	J124610.0+304355	$18.3^{+5.4}_{-4.7}$	H20
6	2043	J124611.24+304321.8	191.54683	30.72275	0.0218	37.2	16.4	J124611.2+304321	$70.6^{+9.0}_{-9.0}$	H20
7	♣	‡*J125929.96+275723.1*	194.87483	27.95644	0.0227	71.3	34.4	J125929.9+275723	$154.2^{+31.3}_{-31.5}$	H20
8	♣	‡*J125934.12+275648.6*	194.89217	27.94683	0.024	71.3	34.4	J125934.1+275648	$334.7^{+30.5}_{-30.2}$	H20
9	12242	‡*J131513.87+442426.4*	198.80779	44.40736	0.0354	50.9	35.9	J131513.8+442426	$14.5^{+4.5}_{-3.9}$	H20
10	12242	J131517.26+442425.5	198.82196	44.40711	0.0355	50.9	35.9	J131517.3+442425	$3835.5^{+65.4}_{-64.8}$	H20
11	2044	J133817.27+481632.1	204.57196	48.27564	0.0278	11.5	6.4	J133817.3+481632	$95.2^{+10.8}_{-10.6}$	Ma12,H20,I20
12	2044	J133817.77+481640.9	204.57404	48.27808	0.0277	11.5	6.4	J133817.8+481640	$205.0^{+15.3}_{-15.2}$	Ma12,H20,I20
13	11845	‡*J150457.12+260058.4*	226.238	26.01625	0.054	61.6	65.2	J150457.1+260058	$68.0^{+9.5}_{-9.4}$	H20
14	11845	‡*J150501.22+260101.5*	226.25508	26.01708	0.0545	61.6	65.2	J150501.2+260101	$15.1^{+4.6}_{-4.0}$	H20
15	14968	‡*J154403.45+044607.5*	236.01437	4.76875	0.042	4.1	3.4	J154403.4+044607	$5.0^{+2.9}_{-2.2}$	H19,H20
16	14968	J154403.66+044610.0	236.01529	4.76947	0.0416	4.1	3.4	J154403.6+044609	$59.3^{+8.2}_{-8.1}$	H19,H20

Note. [(1)–(2)]Angular and projected separation between the sources; [(3)]net observed count in (0.2–12 keV) for 4XMM (EP8) and (2–8 keV) for CSC; [(4)]references: H19, Hou et al. (2019); H20, Hou et al. (2020); K10, Koss et al. (2010); ADR18, De Rosa et al. (2018); I20, Iwasawa et al. (2020); MA12, Mazzarella et al. (2012); R21, Ricci et al. (2021); I11, Iwasawa et al. (2011); TA18, Torres-Albà et al. (2018). †For these sources, we report here the values obtained in De Rosa et al. (2018). ♣ Obs. ID = 9714, 10672, 13993, 13994, 13995, 13996, 14406, 14410, 14411, 14415. Sources in ‡italic are not identified as AGN following our diagnostics (see Section 4).

X-ray sources will be investigated in a forthcoming paper (Parvatikar et al. in preparation).

We note that the dual-AGN sample contains both Seyfert galaxies (or quasars at higher luminosity) and low-ionization nuclear emission-line regions (LINERs), such that pairs are of the types Seyfert–Seyfert, Seyfert–LINER, and LINER–LINER. LINERs are known to be a mixed class of objects with diverse line excitation mechanisms discussed in the literature, such as old stars, shocks, haloes of elliptical galaxies and even intracluster gas, as well as forms of AGN excitation (e.g. Heckman 1980; Shields 1992; Ho, Filippenko & Sargent 1993; Komossa, Böhringer & Huchra 1999). Therefore, not all LINERs are expected to be bona fide AGN. Here, we continue to treat all LINERs as candidate AGN, on a careful object-by-object basis, including information from all optical emission lines. For sources that lie in the composite region of diagnostic diagrams (see Section 3.1) and in the LINER regime, we use the X-ray information to obtain further clues on the main power source of these systems and then re-assess their possible AGN nature in Section 4.

Finally, we would also like to note that the majority of the pairs in our sample are at large projected spatial separations, namely above 10 arcsec (see Table 1). Therefore, the well-known effect of light spillover into nearby fibres owing to seeing, which can mimic AGN pairs when in fact only one AGN is active (Husemann et al. 2020), is minimal in our sample.

3 SPECTRAL ANALYSIS

In this section, we present the MWL spectral analysis of our final sample comprising 26 pairs of dual-AGN candidates (see Table 1). The main objective of this study is to confirm the nature of the selected targets and characterize their intrinsic properties, such as X-ray luminosity, optical over X-ray luminosity ratio, and absorption properties (at nuclear and galactic scales). As illustrated in Section 1, X-ray and mid-IR observations, along with optical spectroscopy, provide fundamental diagnostics for detecting accreting MBHs, even in heavily obscured systems, as expected for dual AGN.

3.1 Optical analysis

We retrieved the SDSS-III DR12 spectra (Alam et al. 2015) at the location of the dual-AGN systems, as reported in Table 1, from the survey webpage.[1] We analysed the full-band optical spectra through the software package QSFIT 1.3.0 (Calderone et al. 2017). This tool automatically takes into account the emission from both AGN and host galaxy, along with a number of broad and narrow emission lines. In particular, we extracted the intensities of the primary diagnostic narrow emission lines such as Hβ, [O III] λ5007, [O I] λ6300, Hα, [N II] λ6583 and [S II] $\lambda\lambda$6717, 6731. Line fluxes were corrected for Galactic extinction using NED (NASA/IPAC Extragalactic Database[2]). The line flux ratios were then plotted in the diagnostic diagrams (Baldwin, Phillips & Terlevich BPT diagram; Kauffmann et al. 2003) shown in Fig. 1 (upper panels refer to *XMM–Newton* sources and bottom panels to *Chandra* sources), where the regions populated with Seyfert galaxies, SF galaxies, and LINERs are identified as in Kewley et al. (2006). The numbers in the plot refer to the sources in Table 1; symbols in the same colour refer to members of a pair. Some of the optical spectra are dominated by the galaxy contribution; however, when possible we also evaluated the extinction $E(B-V)$ considering the Balmer decrement from the narrow emission lines. Sources with at least one BPT diagram indicating an AGN or LINER are included in our sample. There are, however, targets whose optical analysis does not confirm their AGN nature. We kept these sources in the catalogue and will investigate their classification using further diagnostics such as the X-ray luminosity and mid-IR versus X-ray colours in Section 4. We note that only two sources show clear evidence of broad optical lines (J094554.4+423840 and J103853.2+392151; De Rosa et al. 2018), while in the rest of the sample the galactic contribution prevent us from detecting any strong broad-line component.

3.2 X-ray analysis

We reduced *XMM–Newton* data using SAS software v17.0 with standard settings and the most updated calibration files available at the time of the data reduction. Periods of high and flaring background were removed, applying the appropriate threshold on single events extracted above 10 keV (about 0.4 and 0.35 counts per second in EPIC-pn and EPIC-MOS, respectively).

Depending on the source counts and the separation of the two sources in each system, we extracted EPIC spectra from circular regions with radii in the range 11–25 arcsec; these regions include ∼60–90 per cent of the source counts at 1.5 keV in the EPIC cameras. Background spectra were extracted in the same CCD chip using circular regions free from contaminating sources. Owing to the higher net counts in the 0.3–10 keV energy band with respect to EPIC/MOS, we reported the EPIC/pn spectra analysis and checked a posteriori that pn+MOS data do not improve the fit or the spectral parameter constraints. *Chandra* spectra and corresponding response matrices were retrieved from CSC2. When multiple observations of the same source were available, we verified the absence of any sign of variability, and the spectra from the individual observations were merged to increase the S/N ratio (the Obs. ID for each observation is reported in Table 1).

Among the 52 sources, we were able to extract spectral information for 32 targets (4XMM: 17, CSC2: 15). For these sources, EPIC-pn and ACIS background-subtracted spectra were fitted with the software XSPEC v12.10 (Arnaud 1996) using Cash statistics (Cash 1979; Wachter, Leach & Kellogg 1979). We applied a phenomenological model composed of: (1) an absorbed power law – this is the nuclear emission due to the Comptonization of electrons in a hot corona by seed photons, probably originating in the accretion disc (e.g. Haardt & Maraschi 1993; Haardt, Maraschi & Ghisellini 1994); and (2) a soft, unabsorbed power-law component reproducing the extended soft X-ray emission below ∼2 keV, likely associated with the NLR (Bianchi et al. 2019 and references therein), the scattering of the primary emission (Ueda et al. 2007), or star-formation activity (Ranalli, Comastri & Setti 2003). The baseline model can be written as $e^{-N_H^{Gal}\sigma}$ $(e^{-N_H\sigma}K_hE^{-\Gamma_h}+K_sE^{-\Gamma_s})$, where Γ_h and Γ_s are the photon indices of the nuclear primary component and soft X-ray component, respectively; N_H^{Gal} is the Galactic column density; N_H is the cold absorption column density at the redshift of the source; and σ is the photo-absorption cross-section from Balucinska-Church & McCammon (1992). This simple model is sufficient to obtain constraints on the main spectral parameters of interest, such as N_H, Γ, and the unabsorbed luminosity.

If the count statistic does not enable us to constrain Γ_h and Γ_s simultaneously, we put $\Gamma_h=\Gamma_s$, as expected in a scattering model for the soft excess discussed above. We also fixed Γ_h to a typical value

[1] http://skyserver.sdss3.org/
[2] https://ned.ipac.caltech.edu/Documents/References/ExtinctionCalculators

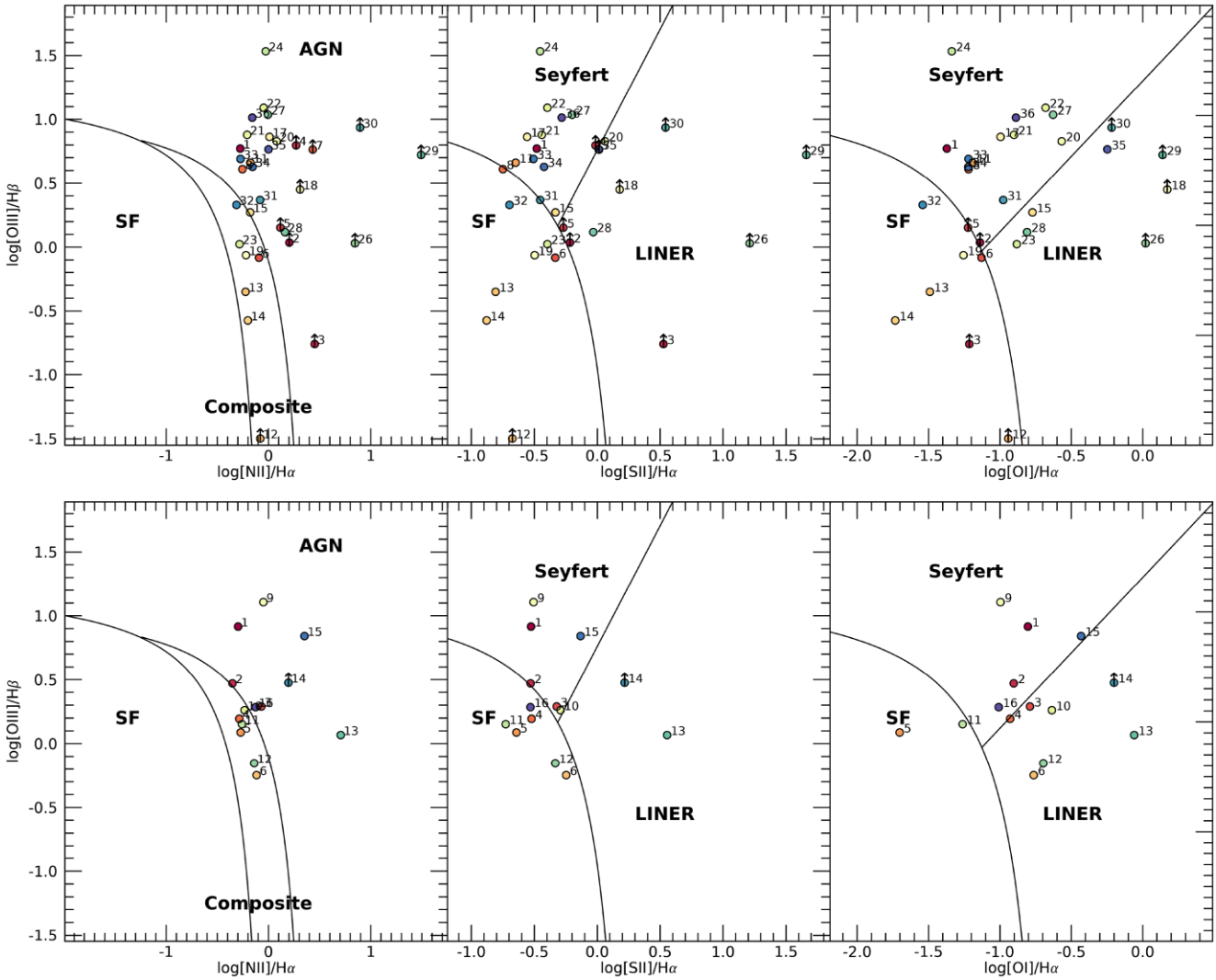

Figure 1. Optical emission-line ratios as classical diagnostic plots for the identification of dual-AGN candidates detected in 4XMM (upper panels) and CSC2 (lower panels). Symbols in the same colour refer to members of a pair. The number of each source is as in Table 1. AGN, LINER and SF regions in the plots are separated according to Kewley et al. (2006).

of 1.9 (Ricci et al. 2017) when the count statistics do not enable us to fit the parameter. The results of the spectral analysis and modelling performed on the sample are reported in Table 2.

4 AGN IDENTIFICATION

We used different diagnostics in order to confirm the AGN nature of our sample against SF galaxies that could produce the observed X-ray luminosity.

At the end of our MWL analysis, we selected 42 confirmed AGN from 52 candidates. For 24 of these AGN we could perform a detailed X-ray spectral modelling, as described in Section 3.2. This 'clean sample' of 24 AGN was then used to calibrate MWL relationships in order to obtain information on the nature (AGN, non-AGN) and absorption properties of the whole sample of 42 dual AGN. Below, we report the details of this study.

As anticipated in the previous section, we retain in the sample targets indicating the presence of an AGN or LINER in at least one optical BPT diagram (see Fig. 1). The X-ray luminosity of the sources associated with LINERs through optical analysis suggests that their emission is powered by the AGN (see Table 2). In fact, a systematic study of a large sample of LINERs identified as unresolved sources at high X-ray energies (4.5–8 keV) suggested that AGN-like objects tend to have higher 2–10 keV luminosities than non-AGN objects, with average values of $\log L_{\rm x}/({\rm erg\ s^{-1}}) \sim 41$ and $\log L_{\rm x}/({\rm erg\ s^{-1}}) \sim 39$, respectively (González-Martín et al. 2009). As a further check to firmly identify AGN, we used the X-ray/mid-IR versus X-ray colours relationship.

In Fig. 2 (left-hand panel), we show the absorption column density versus hardness ratio HR [HR = (H − S)/(H + S), where H and S are the source counts in the soft and hard energy bands], for the 24 sources with spectral information. The hardness ratio HR is evaluated using the S = 2–4.5 keV and H = 4.5–10 keV energy bands for *XMM–Newton* and the S = 0.5–2 keV and H = 2–8 keV for *Chandra*. Sources with larger obscuration are characterized by a larger HR. In particular, in our clean sample, a value of HR larger than about −0.3 indicates a $N_{\rm H} \gtrsim 10^{22}$ cm^{-2} (see Fig. 2, left-hand panel).

Mid-IR emission in AGN is thought to originate within the dusty torus through the reprocessing of optical–UV primary emission

Table 2. X-ray properties of our clean sample of dual-AGN sources detected with *XMM–Newton* and *Chandra*.

IAU name (4XMM/2CXO)	[1]$N_{\rm H}^{\rm Gal}$ (10^{20}cm^{-2})	[2]$N_{\rm H}$ (10^{22}cm^{-2})	[3]$\Gamma_{\rm h}$	[4]$F_{\rm X}^{\rm Obs}$ (10^{-14}erg cm^{-2} s^{-1})	[5]$L_{\rm X}^{\rm Una}$ (10^{40} erg s^{-1})	[6]$L_{[\rm O\,III]}^{\rm corr}$ (10^{40} erg s^{-1})	[7]W4 (mag)	[8]$E(B-V)$ (mag)	[9](X/IR)	[10]Opt
				XMM–Newton						
J082321.6+042221	2.5	$0.6^{+1.4}_{-0.3}$	$3.03^{+0.50}_{-0.44}$	$10.^{+1}_{-1}$	22^{+4}_{-8}	>0.015	8.4	–	U	A
J100135.8+033648	1.9	16^{+31}_{-10}	1.9⋆	$6.3^{+1.1}_{-1.1}$	46^{+15}_{-15}	21.5	6.45 ± 0.05	0.70	t	A
J100236.6+324224	1.3	< 0.4	$2.2^{+0.9}_{-0.6}$	10^{+1}_{-1}	47^{+10}_{-10}	–	8.35	–	U	C
‡*J102142.6+130654*	4.3	< 0.06	1.9⋆	0.8 ± 0.4	10 ± 4	>0.06	4.34 ± 0.04	–	SF	SF
‡*J112545.1+144035*	2.5	$0.2^{+0.4}_{-0.1}$	1.9⋆	$1.2^{+0.2}_{-0.2}$	3.3 ± 1.0	13.6	3.66 ± 0.02	1.3	SF	C
J112549.5+144006	2.4	12^{+55}_{-8}	1.9⋆	1.6 ± 0.3	8.0 ± 0.4	6.3	4.44 ± 0.03	1.3	T	C
J120443.3+311037	1.4	3.7 ± 0.5	1.7 ± 0.4	263 ± 6	309 ± 5	43	3.59 ± 0.02	1.43	t	A
J120445.3+311130	0.44	24^{+150}_{-12}	1.9⋆	$3.0^{+1.1}_{-1.1}$	11^{+7}_{-6}	>0.2	7.92 ± 0.15	–	T	A
J145627.4+211956	2.9	75^{+28}_{-23}	1.9 ± 0.9	$8.6^{+2.0}_{-2.0}$	370^{+20}_{-130}	> 4.5	7.15 ± 0.08	0.35	t	A
J145631.3+212030	2.9	> 100	1.9⋆	$2.3^{+0.5}_{-0.5}$	7 00†	39	5.32 ± 0.03	0.54	T	A
J145838.5+382727	1.2	< 0.6	1.9⋆	$1.2^{+0.2}_{-0.2}$	60 ± 20	46.8	7.34 ± 0.08	0.63	t	A
J162640.9+142243	3.8	67^{+150}_{-50}	1.9⋆	2.3^{+1}_{-1}	80^{+30}_{-70}	31	5.54 ± 0.11	0.44	T	A
J162644.4+142253	3.8	6^{+12}_{-4}	1.9⋆	1.6 ± 0.8	12 ± 0.8	> 0.1	9.04 ± 0.53	–	t	A
J094554.4+423840	1.1	< 0.02	2.4 ± 0.1	50 ± 3	700 ± 30	27.9	5.45 ± 0.04	0.40	U	A
J094554.4+423818	1.1	24^{+8}_{-6}	1.9⋆	19 ± 2	690 ± 30	124	5.84 ± 0.05	0.55	t	A
J103853.2+392151	1.7	< 0.03	1.62 ± 0.07	55 ± 5	420 ± 20	8.0	7.66 ± 0.14	0.33	U	A
J103855.9+392157	1.7	> 100	1.9⋆	1.6 ± 1	700†	19	6.05 ± 0.05	0.30	SF	A
				Chandra						
J090714.4+520343	1.5	18^{+16}_{-12}	1.9⋆	6.4 ± 1.1	160 ± 30	104	6.8 ± 0.1	1.11	t	A
J090714.6+520350	1.5	$2.5^{+1.4}_{-1.1}$	1.5 ± 0.7	13 ± 1	160 ± 1	38	6.8 ± 0.1	0.85	t	A
J121345.9+024838	1.7	<0.56	1.9⋆	$0.7^{+0.2}_{-0.2}$	11 ± 4	46	3.61 ± 0.02	1.48	T/SF	L
J121346.0+024841	1.7	–	2.1 ± 0.6	0.9 ± 0.2	13 ± 3	80	3.61 ± 0.02	1.17	SF	C
‡*J124610.0+304355*	1.16	$0.16^{+0.1}_{-0.8}$	1.9⋆	1.1 ± 0.5	1.4 ± 0.1	5.3	4.08 ± 0.03	1.37	SF	SF
J124611.2+304321	1.16	$0.17^{+0.1}_{-0.1}$	1.9⋆	1.2 ± 0.3	1.5 ± 0.1	0.5	7.4 ± 0.1	0.43	U	C/L
J125934.1+275648	0.9	–	$1.7^{+0.9}_{-0.1}$	<0.67	<1	8.4	–	–		
J131513.8+442426	1.7	–	$3.0^{+1.3}_{-1.1}$	0.055	<0.18	150	6.19 ± 0.05	1.57	SF	A
J131517.3+442425	1.7	$9.5^{+0.5}_{-0.4}$	1.9⋆	330 ± 5	$(1.9^{-2.1}_{-0.8}) \times 10^3$	59	3.43 ± 0.02	0.83	t	C
J133817.3+481632	1.4	>200	1.6 ± 0.3	2.2 ± 0.9	$(1.3^{-2.7}_{-0.8}) \times 10^3$	13.8	2.54 ± 0.01	0.71	SF	C/SF
J133817.8+481640	1.4	6.8 ± 3.8	1.9⋆	24.6 ± 2.0	40.	14.9	2.54 ± 0.01	–	t	C/SF
‡*J150457.1+260058*	3.5	–	1.9⋆	0.2 ± 0.1	1.5 ± 0.2	0.06	8.8 ± 0.1	–	SF	Amb
‡*J150501.2+260101*	3.5	–	$1.1^{+0.9}_{-0.7}$	<0.1	<0.9	0.08	8.8 ± 0.1	–	SF	Amb
‡*J154403.4+044607*	3.9	–	$2.9^{+1.2}_{-1.1}$	<0.1	<0.46	150	6.38 ± 0.07	2	SF	L
J154403.6+044609	3.9	$2.8^{+2.8}_{-1.9}$	$1.3^{+1.2}_{-1.0}$	8.1 ± 0.9	48 ± 9	25	6.38 ± 0.07	1.2	t	L

Note. [1]Galactic hydrogen column density NI from HI4PI Collaboration et al. (2016). [2]Nuclear absorption column density: '–' refers to sources with an upper limit on $N_{\rm H}$ of a few × 10^{20} cm^{-2}. [3]Photon index of the hard power law: values with ⋆ are left fixed in the fit. [4]Observed 0.5–10 keV (4XMM) and 2–8 keV (2CXO) X-ray flux in 10^{-14} erg cm^{-2} s^{-1}. [5]Unobscured 2–10 keV X-ray luminosity in 10^{40}erg s^{-1}. †For Compton-thick sources, we used the relation in Lamastra et al. (2009) and Marinucci et al. (2012): the intrinsic 2–10 keV luminosity was obtained by multiplying the observed luminosity by 70. [6]De-reddened [O III] luminosity in 10^{40}erg s^{-1}. [7]WISE W4 magnitude. [8]Extinction considering the Balmer decrement from narrow emission lines: '–' indicates a source where a precise measure of Hβ has not been obtained (see Section 3.1 for details). [9–10]Source classification following the X/IR versus hardness ratio and optical diagnostics. A, AGN; SF, star-forming; L, LINER; C: composite; U, unabsorbed; t, Compton-thin; T, Compton-thick; Amb, ambiguous. Sources in ‡italic did not pass the check for AGN classification.

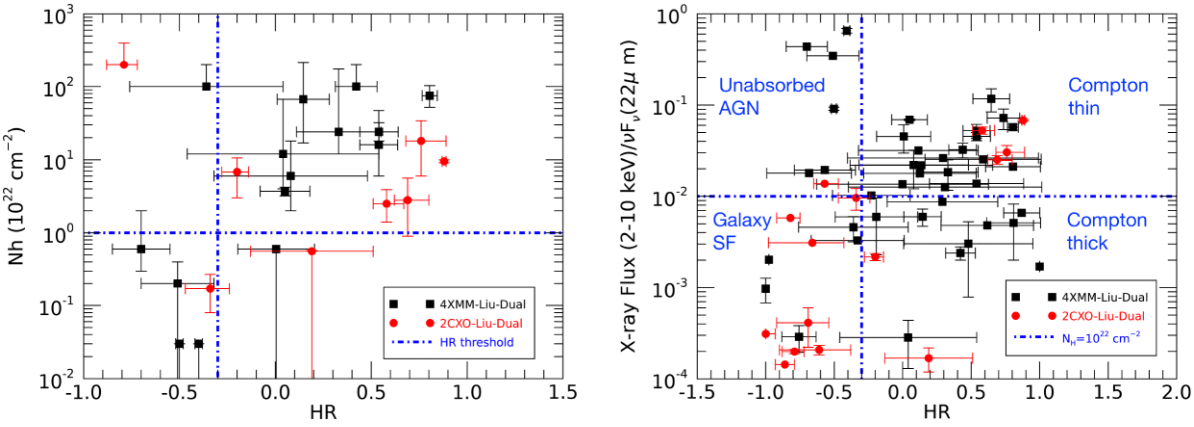

Figure 2. Left: Absorption column density versus hardness ratio, HR = (H – S)/(H + S), for the clean sample of 24 dual AGN with spectral information (see Table 2). HR is evaluated considering $S = 2$–4.5 keV and $H = 4.5$–10 keV for 4XMM data, and $S = 0.5$–2 keV and $H = 2$–8 keV for CSC2 data. The dash–dotted vertical line defines the threshold for sources with $N_H > 10^{22}$ cm^{-2} in our sample. Right: AGN identification and absorption diagnostic using mid-IR versus HR for the total sample of 42 confirmed dual AGN (sse Table 1). Dash–dotted lines identify the regions in the plot where different classes of X-ray and mid-IR emitters are located (Severgnini et al. 2012).

(Padovani et al. 2017 and references therein), and mid-IR colour–colour diagrams offer important diagnostics for identifying AGN candidates. Using classical colour–colour diagrams through WISE 3-bands measurements ([2.4–4.6] μm versus [4.6–12] μm; Mateos et al. 2012; Assef et al. 2013; Yan et al. 2013), our candidates lie roughly in the AGN region ([4.6–12] μm above 2) and tend towards red colours ([2.4–4.6] μm above 0.3), as suggested for AGN in mergers (Satyapal et al. 2014; Weston et al. 2017). Nevertheless, AGN are not the largest population in mid-IR surveys, which are dominated by strong IR emission from SF and normal galaxies. This is the reason why combined mid-IR and X-ray analysis provides further information to confirm AGN candidates (Severgnini et al. 2012; Terashima et al. 2015).

Severgnini et al. (2012) proposed an effective technique to classify AGN and SF galaxies by comparing mid-IR (12–25 μm) and X-ray fluxes. In their diagnostic plot, the X-ray/mid-IR flux ratio is compared with X-ray hardness ratio values, with different regions in the plot hosting different populations (SF galaxies, unobscured AGN, Compton-thin AGN, and Compton-thick AGN). Then we use the ratio F(X-rays)/F(22 μm) versus HR relationship reported in the right-hand panel of Fig. 2 to exclude X-ray-detected targets that are not associated with AGN and evaluate (in Section 5.1) the level of absorption for the sources in the total sample without X-ray spectral information (see Table 1 and Fig. 2, right-hand panel). Using the results of spectral analysis for the sources with high enough counts (our 'clean' sample), we calibrated the X-ray/mid-IR versus HR plot that allowed us also to identify the regions where different types of emitters are expected (details will be presented in Section 5.1): we chose the limit HR > -0.3 (as obtained for obscured sources with $N_H \gtrsim 10^{22}$ cm^{-2}) and, as the X-ray/mid-IR ratio, we adopted a threshold of 0.01 (blue dash–dotted lines in Fig. 2). We note that, given the intrinsic dispersion of the X-ray/mid-IR versus HR relationship, these values are not different from those adopted by Severgnini et al. (2012).

Using optical classification (see Fig. 1) and the X-ray/mid-IR ratio (see Fig. 2, right-hand panel), we identified and confirmed 42 AGN (4XMM: 33 targets, and CSC2: 9 targets), which is 80 per cent of the detected targets in pairs (52). The last two columns in Table 2 report the classification of each source as obtained with the optical and X-ray/mid-IR ratio. The sources that did not pass at least one of the two checks are indicated in italic in Tables 1 and 2; however, when available, we report the results of their X-ray spectral fit for completeness. A peculiar but illustrative case is J133817.3+481632 (aka Arp 266), which is a known Compton-thick AGN hosted in a dual system (Iwasawa et al. 2020; Mazzarella et al. 2012). It appears as a SF galaxy in our X-ray/mid-IR diagnostic plot and BPT (see src # 11 in Fig. 1, lower panel), suggesting that the number of heavily absorbed AGN in our final sample should be considered a lower limit (see further discussion in Section 5.2). A similar case of such a highly obscured system is NGC 6240 (Komossa et al. 2003).

We also note that, for pair candidates detected by *Chandra* (see Table 1), four are at an angular separation below 12 arcsec, which corresponds to the WISE 22-μm resolution (Wright et al. 2010). One of these four systems is the well-known AGN pair Arp 266 that we have just discussed. However, considering the X-ray/mid-IR versus HR diagnostic plot, the decrease of the IR flux (due to blended emission between the two sources) will move the sources in the AGN region, resulting, once again, in a lower limit in our estimated AGN fraction in the final sample.

5 DISCUSSION

5.1 Absorption properties

We were able to extract X-ray spectra and perform a detailed analysis for 32 sources among the 52 AGN candidates in 4XMM and CSC2. The optical and X-ray/mid-IR ratio presented in Section 4 points towards an AGN classification for 24 out of 32 targets. We present the spectral analysis for all 32 sources with best-fitting values in Table 2; however, we excluded from our final considerations on dual-AGN properties all sources (8) that are not confirmed as AGN (reported in italic in Table 2).

In the left-hand panel of Fig. 3, we plot the intrinsic unobscured X-ray luminosity of our dual-AGN sample with spectral information in bins of projected separation rp. A trend of increasing luminosity with decreasing rp is suggested, although it should be noted that the bin rp > 60 kpc is poorly populated (3 AGN) in this analysis, while smaller-separation bins are populated with 10 (0–30 kpc) and 11 (30–60 kpc) targets.

Among the 24 targets with measured N_H, a fraction of 70–74 per cent exhibit an absorption column density higher than 10^{22}

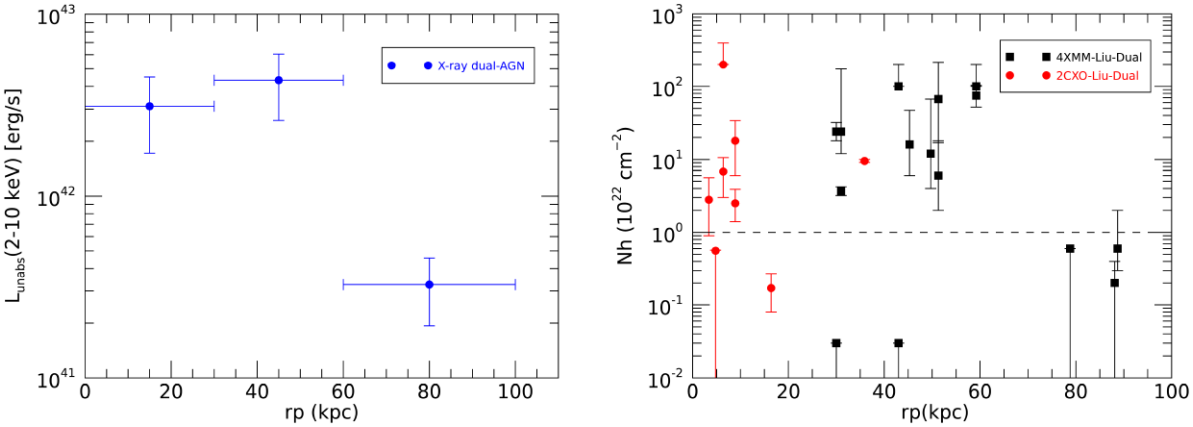

Figure 3. Broad-band intrinsic X-ray luminosity (left-hand panel) and absorbing column density $N_{\rm H}$ (right-hand panel) versus projected separation rp for a clean sample of X-ray dual AGN detected in 4XMM and CSC2 and with spectral information (see Table 2). $L_{\rm unabs}$ errors are dominated by dispersion in each single bin.

cm^{-2} at 3–100 kpc separation (see the right-hand panel in Fig. 3). We measure an upper limit $N_{\rm H} < 3 \times 20$ cm^{-2} for the two AGN showing broad optical emission lines (J094554.4+423840 and J103853.2+392151; De Rosa et al. 2018, see Section 3.1). Although we do not see a clear trend of absorption with rp (but see further discussion below, based on the absorption on the whole sample), we note that there are no absorbed AGN ($N_{\rm H} > 10^{22}$ cm^{-2}) in systems with a projected separation above 60 kpc. The fraction of absorbed AGN in dual systems is larger than that measured in samples of isolated AGN (e.g. 45 per cent in Swift/BAT; Ricci et al. 2015), which is in agreement with previous studies on X-ray dual AGN (Koss et al. 2011; De Rosa et al. 2018; Ricci et al. 2017, 2021). However, we note here that our sample is neither complete nor unbiased in any sense. In order to evaluate the amount of absorption in the 42 X-ray dual AGN, we use indirect measurements. Below, we describe two main proxies for absorption: [O III]/X ratio, X-ray/mid-IR ratio versus hardness ratio.

5.1.1 L_X versus $L_{\rm [O\,III]}$

Once the extinction within the NLR is properly considered, the luminosity of the emission line from [O III]λ5007 can be used as a good indicator of the intrinsic luminosity of the source. In our analysis of optical spectra (Section 3.1), we correct the [O III] emission for the extinction through the Balmer decrement (Hα/Hβ ratio). To derive the $L^{\rm corr}_{\rm [O\,III]}$ corrected for extinction, we used the relationship from Bassani et al. (1999), which assumes the Cardelli, Clayton & Mathis (1989) extinction law and an intrinsic Balmer decrement equal to 3; this value represents the case for the NLR (Osterbrock & Ferland 2006). The values of $L^{\rm corr}_{\rm [O\,III]}$ for the sources with X-ray spectral information are reported in Table 2. The ratio between the observed X-ray luminosity and $L^{\rm corr}_{\rm [O\,III]}$ has therefore been used as an indirect measurement of $N_{\rm H}$. The $L_{\rm x}/L^{\rm corr}_{\rm [O\,III]}$ relationship has been deeply analysed for large samples of type 1 and type 2 AGN (Heckman et al. 2005; Mulchaey et al. 1994; Bassani et al. 1999; Lamastra et al. 2009; Vignali et al. 2010), and empirical trends have been found by several authors.

In Fig. 4, we report the observed X-ray luminosity versus the [O III] luminosity corrected for extinction, $L^{\rm corr}_{\rm [O\,III]}$. For the sources without a measure of Hβ emission, we considered the observed value of [O III], which should then be regarded as a lower limit to $L^{\rm corr}_{\rm [O\,III]}$. As a comparison, we also plot the relationship found by Lamastra et al. (2009) for a sample of Compton-thin AGN. Almost 80 per cent of our sample lies below the threshold as defined in Lamastra et al. (2009), clearly showing that our sources exhibit an excess of absorption with respect to what is expected in isolated Compton-thin AGN. In the X-ray–[O III] plane, the two type 1 AGN in our sample (094554.4+423840 and J103853.2+392151) are located above the relationship defined for obscured sources, as expected.

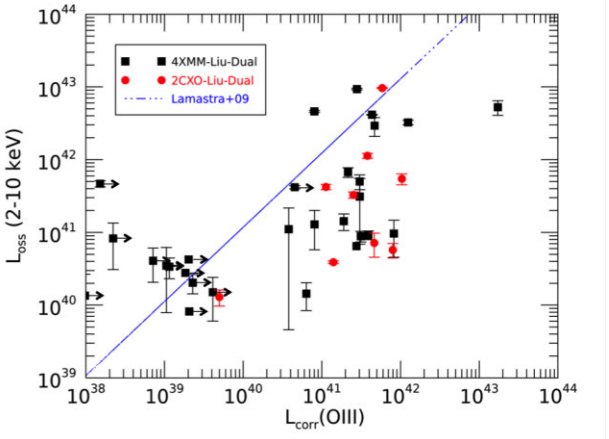

Figure 4. X-ray observed luminosity versus de-reddened [O III] luminosity for the whole sample of confirmed AGN. 4XMM, black squares; CSC2, red circles. Lower limits to $L^{\rm corr}_{\rm [O\,III]}$ refer to the sources without a measure of Hβ emission; for those, we use the observed value of [O III]. The blue dot–dashed line represents the relationship found in Lamastra et al. (2009) for a sample of Compton-thick AGN. All sources in pairs lie below the expected relationship, suggesting a larger absorption with respect to isolated AGN. The two type 1 AGN in the 4XMM sample are the only measured data points above the relationship.

With the caveat that for some sources of the sample only a lower limit to the Hβ emission has been obtained, we can compare the column density derived from $E(B-V)$ – as evaluated from the NLR (see Table 2, Domínguez et al. 2013) and using, for the conversion, the Galactic $N_{\rm H}/E(B-V)$ ratio (Draine 2011) – with the $N_{\rm H}$ measured from the X-ray analysis (excluding type 1 AGN). The extinction in the NLR is lower than the obscuration derived from X-rays, and there is no evidence for a trend of increasing $E(B-V)$ as a function

Table 3. X-ray detection efficiency for optically selected dual AGN. This is the ratio between the detected optically selected AGN and the observed ones in the field of *XMM–Newton* and *Chandra* observations.

Catalogue	[(1)]*Chandra* det./obs. (per cent)	[(1)]*XMM* det./obs. (per cent)	X-ray tot. (per cent) det./obs. (per cent)
$T>10$ ks and $R_{\rm offset}<15$ arcmin (*XMM*)–10 arcmin (*Chandra*)			
Liu et al. (2011)	51/137 (37)	73/165 (44)	124/302 (41)
Mezcua et al. (2014)	5/16 (31)	7/8 (88)	12/24 (50)
Ge et al. (2012)	11/18 (61)	15/17 (88)	26/35 (74)
Wang et al. (2009)	8/10 (80)	2/5 (40)	10/15 (67)
Smith et al. (2010)	14/17 (82)	6/11 (55)	20/28 (71)
Kim et al. (2020)	11/11 (100)	5/6 (83)	16/17 (94)
[(2)]Tot.	100/209/0.8 (60)	108/212/0.8 (64)	208/421/0.8 (62)
$T>15$ ks and $R_{\rm offset}<15$ arcmin (*XMM*)–10 arcmin (*Chandra*)			
[(2)]Tot.	100/154/0.8 (81)	108/152/0.8 (89)	208/306/0.8 (85)

Note. [(1)]Fraction of AGN detected in 4XMM/CSC2 catalogues over those observed for more than 10 ks (upper rows) and 15 ks (last row) considering an off-axis position <10 arcmin for *Chandra* and <15 arcmin for *XMM–Newton*. Exposure time refers to elapsed time. [(2)]The total has been evaluated considering that the number of confirmed AGN is 80 per cent of the observed targets (see details in Section 5.2).

of the separation rp as observed for the X-ray-derived $N_{\rm H}$ in Fig. 3 (right-hand panel). This result suggests that the gas responsible for the X-ray obscuration is probably associated with the torus and/or the BLR (e.g. Padovani et al. 2017).

5.1.2 $F_X/F_{[\rm IR]}$ versus *X-ray hardness ratio*

As anticipated in Section 4, we used the mid-IR/X-ray flux ratio to identify the AGN among the X-ray-detected targets (see Table 1). This ratio, when compared with X-ray colours, provides a powerful diagnostic for obscuration (Severgnini et al. 2012), and also when $N_{\rm H}$ is not available from X-ray fitting procedures. We then use the clean sample with spectral information (24 AGN, see Table 2) to calibrate the $N_{\rm H}$ versus HR relationship to be used in the total sample, as discussed in Section 4 and shown in the left-hand panel of Fig. 2.

The plot X-ray/mid-IR versus HR in the right-hand panel of Fig. 2 allows us to identify four regions for unabsorbed, SF galaxies, Compton-thin and Compton-thick sources. The sources in the bottom-left block are identified as SF galaxies also from optical analysis (see Section 3.1 and Fig. 1). We checked that, within the diagnostic plot, all sources analysed through X-rays and optical analysis are correctly located: in Table 2 we report the identification obtained with all diagnostics, X-rays, optical and X-ray/mid-IR versus HR. We note, however, that J133817.3+481632 (aka Arp 266 SW) and J103855.9+392157, which are Compton-thick, fall in the SF region, with their spectra being dominated by the soft X-ray component with the nuclear emission completely obscured (Iwasawa et al. 2020; De Rosa et al. 2018). This is also in agreement, as anticipated in Section 4, with the optical classification of these targets, but demonstrating that we can miss a number of Compton-thick sources in our final sample of confirmed AGN.

If we consider all 42 confirmed AGN detected in 4XMM (33) and CSC (9) in Fig. 2 (right-hand panel), the mid-IR and X-ray diagnostics suggest that our sample is composed of 80 per cent Compton-thin AGN, 16 per cent Compton-thick, and 4 per cent unobscured sources. As mentioned above, the number of Compton-thick sources can be regarded as a lower limit. If we compare these fractions with isolated AGN, we confirm the trend of more obscured AGN being hosted in pairs. As pointed out above, we do not see a clear trend of increasing $N_{\rm H}$ with decreasing rp (see Fig. 3, left-hand panel). However, the fraction of absorbed AGN in these dual-AGN systems that are in the early stages of merging (projected separation up to 100 kpc) is lower with respect to the fraction of heavily obscured AGN found in systems in the late stages of merging (e.g. Ricci et al. 2021), suggesting the presence of larger reservoir of nuclear gas or with a different distribution in AGN at closer separations.

We note that, as described in the previous section, the bulk of absorption we measure is probably associated with the nuclear scale (BLR/torus). This indicates that the observed systems are in environments where gas is transported closer to the AGN and/or disturbed in dual AGN separated by <60 kpc. Based on the data discussed in this work, we find no strong evidence that AGN pairs with projected separations in the ∼1–100 kpc range prefer gas-rich galaxies (i.e. with a larger fraction of gas mass than other galaxies; Kewley et al. 2006). If confirmed in subsequent observations, this would imply that interactions with gas (via tides, spiral arms, dynamical friction, etc.) are not a necessary mechanism for the orbital evolution of AGN pairs from 100-kpc scales. Samples like the one analysed in this paper could therefore be used to place some initial observational constraints on theoretical models describing the orbital evolution of MBH pairs.

5.2 X-ray detection efficiency for dual-AGN candidates

In this section we evaluate the efficiency of X-ray observations for detecting optically selected dual-AGN candidates. With this aim, we considered the optically selected sample of AGN pairs and measured the ratio between the number of detected optical AGN and the number of observed optical AGN along the *XMM–Newton* and *Chandra* pointings, Xeff=DET/OBS. To increase the available statistics, in addition to the sample of AGN pairs from Liu et al. (2011), we considered further samples of dual AGN identified from both optical image (Mezcua et al. 2014) and double-peaked emission-line (Ge et al. 2012; Wang et al. 2009; Smith et al. 2010; Kim et al. 2020) techniques. The list of the selected samples is reported in Table 3. We

note that almost 90 per cent of X-ray-detected targets in all samples have been observed for more than 10 ks of elapsed time.

Moreover, most of the detected sources have been observed serendipitously, with an off-axis position up to 12–15 arcmin. In order to select the number of observed AGN candidates, we consider here two thresholds: exposure and off-axis position. To take into account the fastest drops of *Chandra* sensitivity at increasing off-axis angles with respect to *XMM–Newton*, we selected all targets in the *XMM–Newton* and *Chandra* field of view with an off-axis position lower than 15 and 10 arcmin, respectively, and with exposure longer than 10 ks. Of course, the number of observed AGN might depend of the threshold we assumed; however, we verified that the numbers reported below are stable against other choices of off-axis position and exposures close to the selected ones.

In Table 3 we report the ratio Xeff of all the optically selected dual AGN detected in 4XMM and CSC2, a row for each optical sample we checked. We stress that these detection fractions should be considered as lower limits for two main reasons. Regarding the numerator of the ratio Xeff (the X-ray-detected optically selected AGN), we note that the upper limit for the undetected sources is in the range 0.004–0.04 cts/s (3σ c.l.) in the 4XMM 2–12 keV band, suggesting that we may fail to detect heavily obscured sources with X-ray luminosity lower than 10^{42} erg s^{-1}, considering an average redshift for our sample of $z = 0.03$ and a standard spectral slope of $\Gamma = 2$. Regarding the denominator, the X-ray-observed optically selected AGN, another important point to consider is the possibility that the optical classification as AGN in the samples under investigation could instead be due to SF emission in the galaxy. In fact, as we showed through our MWL analysis (see Section 4), about 80 per cent of the optically selected targets are confirmed as AGN. If we consider this fraction, the X-ray detection efficiency considering all optically selected dual AGN in 4XMM and CSC2 (last column in Table 3) is about 60 per cent. Increasing the exposure cut to 15 ks, the detection efficiency increases slightly, from 62 to 85 per cent. This suggests that, when observed properly, X-ray data represent a powerful technique to confirm and investigate dual-AGN systems. In this regard, we note that in the sample with a higher X-ray detection fraction (Kim et al. 2020, Mezcua et al. 2014 and Ge et al. 2012 for 4XMM; Wang et al. 2009, Smith et al. 2010 and Kim et al. 2020 for *Chandra*), the average value of the off-axis position of the observed targets is lower than in the sample with low X-ray detection efficiency.

6 CONCLUSIONS

We have investigated the properties in the X-ray domain of a sample of optically selected dual AGN with projected separation between 3 and 97 kpc. Using optical, mid-IR and X-ray diagnostic tools, we were able to characterize the intrinsic properties of this sample and compare them with those of isolated AGN.

(i) Among 124 X-ray-detected dual-AGN candidates, 52 appear in pairs and 72 as single X-ray AGN. We focused our study on AGN detected in pairs, while AGN detected in single sources will be analysed in a forthcoming paper (Parvatikar et al., in preparation).

(ii) Using optical spectroscopy (BPT diagrams in Fig. 1) and X-ray/mid-IR versus X-ray HR (Fig. 2), we confirmed as X-ray dual AGN 42 (80 per cent) sources (either LINER or AGN). The X-ray luminosity of LINER sources strongly favours a scenario in which the source emission is accretion-driven. Owing to the possible identification of heavily obscured AGN as SF galaxies (see e.g. the cases of J133817.3+481632 and J103855.9+392157) and the blended IR emission of unresolved pairs in the W4 band, this fraction should be considered as a lower limit.

(iii) We confirmed the trend of increasing AGN luminosity with decreasing separation (see the left-hand panel of Fig. 3), suggesting that mergers may trigger more luminous AGN.

(iv) When comparing optical (de-reddened [O III]) and observed X-ray luminosities (i.e. not corrected for the obscuration; see Fig. 4), our sample shows, on average, a larger obscuration with respect to the relationship found for obscured Seyfert galaxies in isolated systems. Moreover, systems at closer separation show a higher obscuration with respect to dual AGN with separation rp above 50–60 kpc.

(v) The $N_{\rm H}$ measured from X-ray spectral analysis is always higher than the absorbing column density derived form the extinction $E(B - V)$ evaluated for a NLR, suggesting that the gas responsible from the obscuration should lie in nuclear regions (probably the torus or BLR).

(vi) Using X-ray/mid-IR ratio versus HR (see Fig. 2), we estimate that a fraction of 80 per cent of the confirmed AGN are Compton-thin (with $N_{\rm H}$ higher than 10^{22} cm^{-2}) and 16 per cent are Compton-thick ($N_{\rm H}$ higher than 10^{24} cm^{-2}). These fractions are higher if compared with samples of isolated systems, but lower with respect to the fraction of heavily obscured AGN found in systems in the late stage of the merging process (projected separation below 10–20 kpc). This evidence suggests that pairs of AGN are more heavily obscured with respect to isolated AGN.

(vii) These findings indicate that dual AGN occur in environments where gas is transported closer to the AGN and/or disturbed for dual AGN separated by <60 kpc. If the host galaxies of the dual AGN in this sample are further shown to contain amounts of gas similar to those in galaxies with single AGN, this would suggest that interactions with gas are not a necessary mechanism for the orbital evolution of AGN pairs from 100-kpc scales.

(viii) When different samples of dual AGN are considered, we found that the X-ray detection efficiency (defined as the ratio between the X-ray-detected and observed optical AGN in dual systems) lies in the range of 62–85 per cent, depending on the exposure we considered (10–15 ks, see Table 3). This fraction should be considered as a lower limit because, owing to the limited exposures of X-ray dual systems (mainly observed serendipitously) in the 4XMM and CSC2 catalogues, we miss in our analysis all the heavily obscured AGN with 2–10 keV luminosity lower than 10^{42} erg s^{-1} at $z = 0.03$.

ACKNOWLEDGEMENTS

We would like to thank the referee for their careful reading of the manuscript and useful comments, which helped to improve its quality. We acknowledge a financial contribution from the Bando Ricerca Fondamentale INAF 2022 Large Grant, 'Dual and binary supermassive black holes in the multi-messenger era: from galaxy mergers to gravitational waves'. ADR, PS, CV and SB acknowledge a financial contribution from the agreement ASI-INAF n.2017-14-H.O. MC acknowledges support from NSF AST-200793. This research has made use of data obtained from the 4XMM *XMM–Newton* serendipitous source catalogue compiled by the 10 institutes of the *XMM–Newton* Survey Science Centre selected by the ESA. This research has made use of data obtained from the *Chandra* Source Catalog, provided by the *Chandra* X-ray Center (CXC) as part of the *Chandra* Data Archive. This publication makes use of data products from the Wide-field Infrared Survey Explorer, which is a joint project of the University of California, Los Angeles, and the Jet Propulsion Laboratory/California Institute of Technology, and NEOWISE, which is a project of the Jet Propulsion Lab-

oratory/California Institute of Technology. WISE and NEOWISE are funded by the National Aeronautics and Space Administration. Funding for SDSS-III has been provided by the Alfred P. Sloan Foundation, the Participating Institutions, the National Science Foundation, and the US Department of Energy Office of Science. The SDSS-III website is http://www.sdss3.org/. SDSS-III is managed by the Astrophysical Research Consortium for the Participating Institutions of the SDSS-III Collaboration, including the University of Arizona, the Brazilian Participation Group, Brookhaven National Laboratory, Carnegie Mellon University, University of Florida, the French Participation Group, the German Participation Group, Harvard University, the Instituto de Astrofisica de Canarias, the Michigan State/Notre Dame/JINA Participation Group, Johns Hopkins University, Lawrence Berkeley National Laboratory, Max Planck Institute for Astrophysics, Max Planck Institute for Extraterrestrial Physics, New Mexico State University, New York University, Ohio State University, Pennsylvania State University, University of Portsmouth, Princeton University, the Spanish Participation Group, University of Tokyo, University of Utah, Vanderbilt University, University of Virginia, University of Washington, and Yale University.

DATA AVAILABILITY

The high-level data underlying this article were extracted through standard processing from raw data stored in public archives (SDSS, *XMM–Newton*, *Chandra* and WISE), and will be shared on reasonable request to the corresponding author.

REFERENCES

Alam S. et al., 2015, ApJS, 219, 12
Amaro-Seoane P. et al., 2022, accepted for publication in Living Reviews in Relativity (arXiv:2203.06016)
Arnaud K. A., 1996, in Jacoby G. H., Barnes J., eds, ASP Conf. Ser. Vol. 101, Astronomical Data Analysis Software and Systems V. Astron. Soc. Pac., San Francisco, p. 17
Assef R. J. et al., 2013, ApJ, 772, 26
Ballo L., Braito V., Della Ceca R., Maraschi L., Tavecchio F., Dadina M., 2004, ApJ, 600, 634
Balucinska-Church M., McCammon D., 1992, ApJ, 400, 699
Bassani L., Dadina M., Maiolino R., Salvati M., Risaliti G., Della Ceca R., Matt G., Zamorani G., 1999, ApJS, 121, 473
Bianchi S., Chiaberge M., Piconcelli E., Guainazzi M., Matt G., 2008, MNRAS, 386, 105
Bianchi S., Guainazzi M., Laor A., Stern J., Behar E., 2019, MNRAS, 485, 416
Blecha L., Snyder G. F., Satyapal S., Ellison S. L., 2018, MNRAS, 478, 3056
Burke-Spolaor S., 2011, MNRAS, 410, 2113
Calderone G., Nicastro L., Ghisellini G., Dotti M., Sbarrato T., Shankar F., Colpi M., 2017, MNRAS, 472, 4051
Capelo P. R., Dotti M., Volonteri M., Mayer L., Bellovary J. M., Shen S., 2017, MNRAS, 469, 4437
Cardelli J. A., Clayton G. C., Mathis J. S., 1989, ApJ, 345, 245
Cash W., 1979, ApJ, 228, 939
Comerford J. M., Gerke B. F., Stern D., Cooper M. C., Weiner B. J., Newman J. A., Madsen K., Barrows R. S., 2012, ApJ, 753, 42
De Rosa A. et al., 2015, MNRAS, 453, 214
De Rosa A. et al., 2018, MNRAS, 480, 1639
De Rosa A. et al., 2019, New Astron. Rev., 86, 101525
Di Matteo T., Springel V., Hernquist L., 2005, Nature, 433, 604
Domínguez A. et al., 2013, ApJ, 763, 145
Draine B. T., 2011, Physics of the Interstellar and Intergalactic Medium. Princeton University Press
Evans I. N. et al., 2010, ApJS, 189, 37
Evans I. N. et al., 2020, in Am. Astron. Soc. Meeting Abstr., Vol. 235. p. 154.05
Foord A., Gültekin K., Nevin R., Comerford J. M., Hodges-Kluck E., Barrows R. S., Goulding A. D., Greene J. E., 2020, ApJ, 892, 29
Fu H., Myers A. D., Djorgovski S. G., Yan L., Wrobel J. M., Stockton A., 2015, ApJ, 799, 72
Ge J.-Q., Hu C., Wang J.-M., Bai J.-M., Zhang S., 2012, ApJS, 201, 31
González-Martín O., Masegosa J., Márquez I., Guainazzi M., Jiménez-Bailón E., 2009, A&A, 506, 1107
Guainazzi M., Piconcelli E., Jiménez-Bailón E., Matt G., 2005, A&A, 429, L9
Guainazzi M. et al., 2021, MNRAS, 504, 393
Haardt F., Maraschi L., 1993, ApJ, 413, 507
Haardt F., Maraschi L., Ghisellini G., 1994, ApJ, 432, L95
Heckman T. M., 1980, A&A, 87, 152
Heckman T. M., Ptak A., Hornschemeier A., Kauffmann G., 2005, ApJ, 634, 161
HI4PI Collaboration et al., 2016, A&A, 594, A116
Ho L. C., Filippenko A. V., Sargent W. L. W., 1993, ApJ, 417, 63
Hopkins P. F., Hernquist L., Cox T. J., Di Matteo T., Robertson B., Springel V., 2006, ApJS, 163, 1
Hou M., Liu X., Guo H., Li Z., Shen Y., Green P. J., 2019, ApJ, 882, 41
Hou M., Li Z., Liu X., 2020, ApJ, 900, 79
Husemann B., Heidt J., De Rosa A., Vignali C., Bianchi S., Bogdanović T., Komossa S., Paragi Z., 2020, A&A, 639, A117
Iwasawa K. et al., 2011, A&A, 529, A106
Iwasawa K. et al., 2020, A&A, 640, A95
Jarrett T. H. et al., 2011, ApJ, 735, 112
Kauffmann G. et al., 2003, MNRAS, 346, 1055
Kewley L. J., Groves B., Kauffmann G., Heckman T., 2006, MNRAS, 372, 961
Kim D. C., Yoon I., Evans A. S., Kim M., Momjian E., Kim J. H., 2020, ApJ, 904, 23
Kocevski D. D. et al., 2012, ApJ, 744, 148
Kocevski D. D. et al., 2015, ApJ, 814, 104
Komossa S., Böhringer H., Huchra J. P., 1999, A&A, 349, 88
Komossa S., Burwitz V., Hasinger G., Predehl P., Kaastra J. S., Ikebe Y., 2003, ApJ, 582, L15
Koss M., Mushotzky R., Veilleux S., Winter L., 2010, ApJ, 716, L125
Koss M. et al., 2011, ApJ, 735, L42
Koss M., Mushotzky R., Treister E., Veilleux S., Vasudevan R., Trippe M., 2012, ApJ, 746, L22
Lamastra A., Bianchi S., Matt G., Perola G. C., Barcons X., Carrera F. J., 2009, A&A, 504, 73
Liu X., Shen Y., Strauss M. A., Hao L., 2011, ApJ, 737, 101
Mannucci F. et al., 2022, Nat. Astron., 6, 1185
Marinucci A., Bianchi S., Nicastro F., Matt G., Goulding A. D., 2012, ApJ, 748, 130
Mateos S. et al., 2012, MNRAS, 426, 3271
Mazzarella J. M. et al., 2012, AJ, 144, 125
Mezcua M., Lobanov A. P., Mediavilla E., Karouzos M., 2014, ApJ, 784, 16
Mulchaey J. S., Koratkar A., Ward M. J., Wilson A. S., Whittle M., Antonucci R. R. J., Kinney A. L., Hurt T., 1994, ApJ, 436, 586
Osterbrock D. E., Ferland G. J., 2006, Astrophysics of Gaseous Nebulae and Active Galactic Nuclei, 2nd edn., University Science Books, Mill Valley, CA
Padovani P. et al., 2017, A&AR, 25, 2
Pfeifle R. W. et al., 2019, ApJ, 875, 117
Piconcelli E. et al., 2010, ApJ, 722, L147
Ranalli P., Comastri A., Setti G., 2003, A&A, 399, 39
Ricci C., Ueda Y., Koss M. J., Trakhtenbrot B., Bauer F. E., Gandhi P., 2015, ApJ, 815, L13
Ricci C. et al., 2017, MNRAS, 468, 1273
Ricci C. et al., 2021, MNRAS, 506, 5935
Satyapal S., Ellison S. L., McAlpine W., Hickox R. C., Patton D. R., Mendel J. T., 2014, MNRAS, 441, 1297
Satyapal S. et al., 2017, ApJ, 848, 126
Severgnini P., Caccianiga A., Della Ceca R., 2012, A&A, 542, A46

Shields J. C., 1992, ApJ, 399, L27
Silverman J. D. et al., 2011, ApJ, 743, 2
Smith K. L., Shields G. A., Bonning E. W., McMullen C. C., Rosario D. J., Salviander S., 2010, ApJ, 716, 866
Terashima Y., Hirata Y., Awaki H., Oyabu S., Gandhi P., Toba Y., Matsuhara H., 2015, ApJ, 814, 11
Torres-Albà N. et al., 2018, A&A, 620, A140
Treister E., Schawinski K., Urry C. M., Simmons B. D., 2012, ApJ, 758, L39
Ueda Y. et al., 2007, ApJ, 664, L79
Vignali C., Alexander D. M., Gilli R., Pozzi F., 2010, MNRAS, 404, 48
Volonteri M., Pfister H., Beckmann R., Dotti M., Dubois Y., Massonneau W., Musoke G., Tremmel M., 2022, MNRAS, 514, 640
Wachter K., Leach R., Kellogg E., 1979, ApJ, 230, 274
Wang J.-M., Chen Y.-M., Hu C., Mao W.-M., Zhang S., Bian W.-H., 2009, ApJ, 705, L76
Webb N. A. et al., 2020, A&A, 641, A136
Weston M. E., McIntosh D. H., Brodwin M., Mann J., Cooper A., McConnell A., Nielsen J. L., 2017, MNRAS, 464, 3882
Wright E. L. et al., 2010, AJ, 140, 1868
Yan L. et al., 2013, AJ, 145, 55

This paper has been typeset from a TEX/LATEX file prepared by the author.